Radial velocity variability of Proxima Centauri: spots and planets

Mikko Tuomi[1,★], Thomas Hackman[1], Jyri Lehtinen[1,2], José I. Vinés[3], Kosti Koistinen[4], Hugh R. A. Jones[5], and James S. Jenkins[6,7]

[1] University of Helsinki, Department of Physics, PO Box 64, 00014, Finland

[2] University of Turku, Finnish Centre for Astronomy with ESO (FINCA), Vesilinnantie 5, 20014, Finland

[3] Departamento de Astronomía, Universidad de Chile, Casilla 36-D, Santiago, Chile

[4] University of Turku, Department of Physics and Astronomy, FI-20014, Finland

[5] University of Hertfordshire, Center for Astrophysics, College Lane Campus, Hatfield, Hertfordshire, UK, AL10 9AB

[6] Universidad Diego Portales, Instituto de Estudios Astrofísicos, Facultad de Ingeniería y Ciencias, Av. Ejército 441, Santiago, Chile

[7] Centro de Astrofísica y Tecnologías Afines (CATA), Casilla 36-D, Santiago, Chile

ABSTRACT

Context. The nearest star to the Sun, Proxima Centauri, is a host to a planetary system. Although one of the proposed candidate planets, Proxima b, has observational Doppler spectroscopic support from three instruments, the other two detections have been either made based on data from one instrument only or recently disputed.
Aims. We perform an analysis of combined ESPRESSO, HARPS, and UVES data in order to verify the existence of the signals of all three candidates.
Methods. We account for various sources of variability in the radial velocities, including correlated noise, colour dependent variability, and rotation-induced periodic variations such as variability caused by star spots.
Results. Our analysis of the combined data reveals evidence for spot structures on the stellar surface, that the long-period candidate c is not supported by the observations, candidate d is confidently detected, and the presence of a new signal at a period of roughly 0.63 days is revealed. If caused by a planet orbiting the star, this short-period signal with an amplitude of 0.205±0.042 ms^{-1} would correspond to a candidate planet with a minimum mass of only 0.067±0.014 M$_{\oplus}$.

Key words. stars: individual: Proxima Centauri – methods: Statistical – techniques: radial velocities – stars: rotation – starspots

1. Introduction

Since the discovery of Proxima Centauri b (Anglada-Escudé et al. 2016), a plethora of studies have been published regarding the observed properties of the star (Ribas et al. 2016, 2017; Davenport et al. 2016; Pavlenko et al. 2017; Vida et al. 2019) and its planetary system (Bixel & Apai 2017; Damasso & Del Sordo 2017; Damasso et al. 2020; Kane et al. 2017; Kervella et al. 2020; Suárez Mascareño et al. 2020; Faria et al. 2022). Evidence has been presented in favour of another long-period candidate Proxima c orbiting the star (Damasso et al. 2020) as well as a third object Proxima d interior to the orbit of Proxima b (Suárez Mascareño et al. 2020; Faria et al. 2022). The radiation and space weather environment of the planets in the system has been studied in detail (Ribas et al. 2017; Garraffo et al. 2022), as well as the structure (Herath et al. 2021; Noack et al. 2021), climate (Boutle et al. 2017; Lee et al. 2021) and prospects of habitability of Proxima b (Del Genio et al. 2019; Meadows et al. 2019; Abrevaya et al. 2020). There is even evidence for an outer dust disk in the system (Anglada et al. 2017). It has also been demon-

strated that Proxima Centauri is indeed gravitationally bound to the nearby α Centauri binary (Kervella et al. 2017).

Proxima Centauri is a flare star (Davenport et al. 2016; Howard et al. 2018; MacGregor et al. 2018; Pavlenko et al. 2019; Vida et al. 2019; Zic et al. 2020), and the frequent flaring has posed problems for attempts to identify whether Proxima b transit the star or not (Kipping et al. 2017; Jenkins et al. 2019; Gilbert et al. 2021). Some candidate transit events have been reported (Kipping et al. 2017; Liu et al. 2018) but their interpretation as transits of planets has not been verified (Blank et al. 2018). Yet, regardless of these difficulties, the transiting nature of Proxima b has been credibly ruled out (Jenkins et al. 2019; Gilbert et al. 2021). This makes it difficult to assess the properties of this nearest low-mass exoplanet orbiting its stellar host in the so-called liquid-water habitable zone (Anglada-Escudé et al. 2016; Ribas et al. 2016). Direct imaging would be a possibility for obtaining information on Proxima c given the proximity of the target star and a larger angular separation, but nothing has been conclusively detected (Mesa et al. 2017; Gratton et al. 2020) and imaging the two short-period candidates b and d remains beyond current capabilities. The existence of candidate Proxima c has elevated credibility due to supporting astrometric evidence

---

from Hubble Space Telescope Fine Guidance Sensors (Benedict & McArthur 2020), but there is also a claim that its radial velocity signal is spurious (Artigau et al. 2022). Fortunately, the end-of-mission Gaia astrometry may be able to provide further insights as the proposed candidate c is detectable in principle according to Kervella et al. (2022).

Yet, questions remain regarding the architecture of the system, i.e., whether the signals corresponding to candidates c and d are really genuine planets in the system and not some artefacts of instrumentation and/or stellar activity. Indeed, doubt has been cast on the existence of the long-period candidate Proxima c (Artigau et al. 2022). This warrants a re-analysis of the radial velocity data with models and methods independent of those applied by e.g. Faria et al. (2022) and Artigau et al. (2022).

Proxima Centauri is also a spotted star. In particular, co-rotation of spots on the stellar surface has enabled determination of the stellar rotation period rather accurately based on photometry (Kiraga & Stepien 2007; Wargelin et al. 2017). Evidence for a 7-year magnetic activity cycle and differential rotation have also been presented based on photometric data and the existence of differential rotation appears rather clear because the star's photometric rotation period varies between 77.1 and 90.1 days (Wargelin et al. 2017). These observations seem broadly consistent with magnetohydrodynamic simulations of the star (Yadav et al. 2016) and those of such fully convective stars in general (Käpylä 2021). Yet, such variability, especially when strongly present in the radial velocities, can also obscure and/or distort planetary signals if not accounted for.

We aim at combining the available radial velocities of Proxima Centauri and re-analysing them in order to test the evidence for the candidate companions c and d, and to search for additional signals in the existing data from ESPRESSO (Faria et al. 2022), HARPS (Anglada-Escudé et al. 2016), and UVES (Butler et al. 2019). In particular, we analyse the available radial velocity data with the moving average (MA) models and delayed-rejection adaptive-Metropolis (DRAM) sampling algorithms whose combination was found to yield the least false positives and negatives in a blind test (Dumusque et al. 2017).

We also assess the nature of the rotation-induced variability in the radial velocities by constructing a physical model of spots co-rotating on the stellar surface. There have been attempts to model spot-induced radial velocity variations with a geometric spot model (Dumusque 2014) and the basics of such models are well-understood (Reiners et al. 2010; Aigrain et al. 2012). Simulations also indicate that radial velocity variations induced by solitary spots can be considerable in magnitude, far exceeding the amplitudes of radial velocity signals of small planets (Korhonen et al. 2014; Andersen & Korhonen 2015; Lisogorskyi et al. 2020).

1.1. Stellar properties

Proxima Centauri is a fully convective low-mass red dwarf of spectral class M5.5 V. We have tabulated some of its relevant physical parameters in Table 1. We adopt a mass of 0.122±0.003 $M_{\oplus}$ (Ribas et al. 2017) to obtain estimates for planetary minimum masses and semi-major axes.

The rotation period of the star has been estimated independently several times. Analyses of ground-based photometry and spectral activity indicators appears to converge around 83 days (Kiraga & Stepien 2007; Wargelin et al. 2017; Collins et al. 2017), and a majority of estimates appear to be consistent with this value (e.g. Suárez Mascareño et al. 2016; Klein et al. 2021), including the current work (Section 2.1). Knowing this funda-

Table 1. Relevant stellar parameters of Proxima Centauri.

Parameter	Estimate	Reference
Spectral Type	M5.5 V	Boyajian et al. (2012)
π (mas)	768.067±0.050	Gaia Collaboration (2021)
$R_{\star}$ ($R_{\odot}$)	0.1542±0.0045	Mann et al. (2015, 2016)
$R_{\star}$ ($R_{\odot}$)	0.146±0.007	Ribas et al. (2017)
$M_{\star}$ ($M_{\odot}$)	0.1221±0.0022	Mann et al. (2015, 2016)
$M_{\star}$ ($M_{\odot}$)	0.122±0.003	Ribas et al. (2017)
$P_{\rm rot}$ (days)	82.5	Kiraga & Stepien (2007)
$P_{\rm rot}$ (days)	82.6±0.1	Collins et al. (2017)
i (deg)	47±7	Klein et al. (2021)

mental period of the star is important because e.g. co-rotation of spots on the stellar surface can cause periodic red- and blueshifts into the determined radial velocities, thus mimicking planetary signals, but also revealing information on the stellar spot structure. We note that Klein et al. (2021) obtained an estimate for the inclination of the stellar rotation axis of 47±7 deg. Given co-planarity of the plane of the rotation axis and the orbits of the planets, this would imply that planetary transits do not occur, which appears to be the observed reality (Jenkins et al. 2019; Gilbert et al. 2021). However, spin-orbit misalignment cannot be ruled out and the estimate for inclination of the stellar axis of spin is based on Zeeman-Doppler imaging, which makes it only a suggestive estimate.

2. Statistical methods

We model the radial velocity variations by applying a model with Keplerian signals, reference velocities and linear or polynomial trend, correlations between velocities and activity indicators, and a moving-average (MA) component accounting for correlated noise (see e.g. Butler et al. 2017; Díaz et al. 2018; Tuomi et al. 2018). The data analyses are conducted by applying the delayed-rejection adaptive-Metropolis (DRAM) posterior sampling methods (Haario et al. 2001, 2006), which is a generalisation of the common Metropolis-Hastings sampling algorithm (Metropolis et al. 1953; Hastings 1970). This sampler enables obtaining estimates for model parameters by identifying areas in the probability space with the highest probability.

We explain here briefly how the DRAM algorithm of Haario et al. (2006) functions. Assume that a parameter vector θ_{i-1} is drawn from a proposal density $q_1(\theta_{i-1}, \theta_i)$. We call parameter θ_{i-1} the current state. According to the Metropolis-Hastings algorithm (Metropolis et al. 1953; Hastings 1970), the acceptance probability for this new vector θ_i is

$$\alpha_1(\theta_{i-1}, \theta_i) = \min \left\{ 1, \frac{\pi(\theta_i|m)q_1(\theta_i, \theta_{i-1})}{\pi(\theta_{i-1}|m)q_1(\theta_{i-1}, \theta_i)} \right\}, \quad (1)$$

where $\pi(\theta|m)$ is the posterior probability density.

If the proposed vector θ_i is rejected, the DRAM algorithm does not set $\theta_i = \theta_{i-1}$ (i.e., the chain does not necessarily "stay" at θ_{i-1}), but another vector θ_i' is proposed by drawing it from a new proposal density $q_2(\theta_{i-1}, \theta_i, \theta_i')$ that depends on both the current state θ_{i-1} and the rejected state θ_i.

This proposed vector θ'_i is then accepted with the probability

$$
\alpha_2(\theta_{i-1}, \theta_i, \theta'_i) = \min \left\{ 1, \frac{\pi(\theta'_i|m)q_1(\theta'_i, \theta_i)}{\pi(\theta_{i-1}|m)q_1(\theta_{i-1}, \theta_i)} \right.
$$
$$
\left. \times \frac{q_2(\theta'_i, \theta_i, \theta_{i-1})[1 - \alpha_1(\theta'_i, \theta_i)]}{q_2(\theta_{i-1}, \theta_i, \theta'_i)[1 - \alpha_1(\theta_{i-1}, \theta_i)]} \right\}. \tag{2}
$$

If the proposed vector θ'_i is also rejected, additional proposals can be tested recursively according to the formulation of Haario et al. (2006). The delayed rejection ends when a vector is accepted and θ_i is set equal to it as the next member of the Markov chain. If none of the proposed vectors get accepted, θ_i is set equal to θ_{i-1}.

We set the proposal density q_1 such that it is a multivariate Gaussian probability density (Haario et al. 2001). We then choose q_2 such that we decrease the covariance of the proposal vector in the dimension of the period parameter of the signal by dividing the corresponding row and column of the covariance matrix by a factor of ten (this corresponds to choosing $\gamma_i = 0.1$ in Section 4 of Haario et al. 2006, for the Keplerian period parameter). In practice, this approach ensures that we are proposing values in the vicinity of θ_{i-1} rather than values far from it in the period space. For instance, if the Markov chain has identified a vector θ_{i-1} such that it has a higher probability than a vast majority of other proposed values (hence decreasing the acceptance rate), we choose to draw samples closer to the corresponding high-probability period in order to detect the corresponding probability maximum in the period space. This is a subjective choice made in order to probe the narrow probability maxima typically encountered in the period space when searching for periodic Keplerian signals.

We conduct the analyses in two stages. First, we apply the DRAM samplings in order to estimate the shape of the posterior probability density as a function of the period of the Keplerian signal. These samplings are performed to identify the positions of the highest probability maxima in the period space that would correspond to candidate signals. The proposed approach corresponds to the common method of searching for periodicities by calculating periodograms of the data (e.g. Lomb 1976; Scargle 1982; Cumming 2004). However, our approach is more general than the more traditional periodograms because rather than calculating model residuals by subtracting other modelled sources of variability, such as other Keplerian signals or activity-induced variations, we treat all model parameters as free parameters when performing the searches (see Anglada-Escudé & Tuomi 2015).

We also apply local samplings in order to detect the exact positions of the identified probability maxima. The idea is that when the Markov chain has identified a narrow probability maximum that cannot be efficiently sampled with the DRAM because almost all proposals are likely to be rejected (in practice when acceptance rate falls below 10^{-2} in the DRAM algorithm), we decrease the width of the proposal density by a factor of 10^3 in the dimension of the period parameter. This modified proposal is then used to draw a sample of 10^4 in our setting such that it probes the neighbourhood of the identified maximum. After this local sampling, we continue by choosing the next state of the chain randomly from the period space to ensure that the chain visits all areas of the period space even in the presence of one or more high-probability maxima. We note that this local sampling violates the ergodicity of the chain such that the corresponding results cannot be used for e.g. parameter estimation. However, it still enables us to accurately probe the period space such that we can estimate the shape of the posterior density as a function

of the period of the Keplerian signal in order to detect the most prominent candidate signals.

In order to ensure that the parameter estimates are trustworthy, we test whether it could be shown that the Markov chains are not close to their stationary distributions by comparing several (at least three) chains. This is performed by applying the Gelman-Rubin statistics (Gelman et al. 2003) for the nonconvergence of the chains (see e.g. Ford 2006). In practice, we compare the variances within and between chains such that we only accept chains for which the Gelman-Rubin statistics R (see Eq. (25) in Ford 2006) has a value below 1.1. This indicates that it cannot be shown that there is a significant difference in the variances within and between chains. We increased the chain lengths such that this criterion was always satisfied. Typically sufficient chain lengths were of the order of 10^7 for models with more than three dozen parameters but much lower values of 10^5 were sufficient for the simplest models.

Having identified the most significant probability maxima in the period space, we then carried on to assess their significances and estimate parameters with additional AM samplings. For this purpose, we obtained Markov chains such that their initial states were chosen to be in the vicinity of the identified signals in the period space. We then tested whether the corresponding candidate signals were statistically significantly detected and satisfied our signal detection criteria. We consider a signal significantly detected in the data if (1) the period parameter is constrained from above and below and the signal can thus be considered periodic; (2) the signal amplitude is statistically significantly greater than zero; and (3) the posterior probabilities of the model $\mathcal{M}_{k+1}$ containing the signal and a reference model $\mathcal{M}_k$ without it satisfy

$$
P(\mathcal{M}_{k+1}|m) \geq \beta P(\mathcal{M}_k|m), \tag{3}
$$

where $P(\mathcal{M}_k|m)$ is the posterior probability of the model given the data m defined as

$$
P(\mathcal{M}_k|m) = \frac{P(m|\mathcal{M}_k)P(\mathcal{M}_k)}{\sum_j P(m|\mathcal{M}_j)P(\mathcal{M}_j)}, \tag{4}
$$

where $P(m|\mathcal{M}_k)$ denotes the integrated likelihood in favour of the model $\mathcal{M}_k$ and $P(\mathcal{M}_k)$ is its prior probability that we assume to be equal for all models. The summation in Eq. (4) is over all tested models, i.e., models with j Keplerian signals with $j = 0, 1, ...$ as well as models with different descriptions for statistical noise and correlations.

The model comparisons were performed by calculating the Bayesian information criteria (BIC) values (e.g. Liddle 2007) and the corresponding probabilities. Although this does not enable estimating the integrated likelihoods accurately, the BIC values still provide a trustworthy method for selecting the best models in practice (see Feng et al. 2016). Following Feng et al. (2016) we choose the threshold such that $\beta = 150$, which can be interpreted as "strong evidence" according to (Kass & Raftery 1995).

Finally, we aimed at simplifying each model according to the principle of parsimony as much as was possible. For instance, if the linear trend parameter was not statistically significantly different from zero, we eliminated it from the model thus decreasing the degrees of freedom and number of parameters in the model. Likewise, if the Keplerian signal had an eccentricity that was not statistically significantly different from zero, we adopted a model with zero eccentricity thus eliminating two free parameters from the model. Such simplifications were tested by looking at the respective model probabilities and ensuring that a simpler model indeed had a higher probability due to the fact that more complicated models are penalised by the Occam's razor.

2.1. Rotation-induced variability

The rotation-induced variability is clearly present in the ESPRESSO radial velocities (see Suárez Mascareño et al. 2020; Faria et al. 2022). As there are no clear correlations between the radial velocities and FWHM values, it becomes necessary to model this rotation-induced variability in radial velocity data rather than attempt to filter in out. We expect the activity-induced variability to be primarily caused by star spots that co-rotate on the stellar surface in and out of view. A star spot at the receding (approaching) part of the stellar surface would lead to an observable blueshift (redshift) given a sufficiently large spot. The modelling of such spots seems appropriate when considering the brightness variability of the star (Benedict et al. 1998; Kiraga & Stepien 2007). This was also the approach of Faria et al. (2022), albeit their methodology and models differ from those applied in the current work. The same periodic behaviour is also present in ESPRESSO FWHM values, as observed by Faria et al. (2022).

Periodic behaviour of FWHM values and photometry imply that sinusoidal functions can be used to describe the spot-induced variations. However, the variations are unlikely to be strictly sinusoidal. This would suggest applying a set of harmonic sinusoids with periods $\frac{P_r}{1}, \frac{P_r}{2}, \frac{P_r}{3}, ...$ to represent a viable candidate model because its first terms correspond to a series approximation of any periodic function. Alternatively, we also consider the possibility that differential rotation plays a role and use sinusoids with periods close to the observed photometric rotation period of the star.

But periodic signals caused by co-rotation of spots on the stellar surface have a distinctive shape that can also be modelled. We attempt to construct a simple physical model for this variability. Geometrically, a small spot on the stellar surface will be visible when $\cos \delta(t)$, defined as

$$\cos \delta(t) = \cos i \sin \psi + \sin i \cos \psi \cos\left(\frac{2\pi t}{P} + \omega\right), \qquad (5)$$

is positive. We focus on the geometrical effects and neglect limb darkening (and other second-order effects) because we do not expect the data precision and observational cadence to enable constraining its magnitude. Changes in the observed radial velocity can thus be described roughly according to

$$g(t) = A \cos \delta(t) \cos \psi \sin i \sin\left(\frac{2\pi t}{P} + \omega\right), \qquad (6)$$

when the corresponding spot is visible (see e.g. Aigrain et al. 2012). In this model, the parameters are inclination of the rotation axis i, spot latitude ψ, phase ϕ, and effect amplitude A that is proportional to the equatorial rotational velocity and depends on spot size and temperature contrast. This equation is a gross simplification and assumes a small uniform spot, but given a sufficiently clear spot structure with a high contrast the model can be expected to function reasonably well. The superposition of several such spots, even accounting for differential rotation, can also be constructed with ease.

3. ESPRESSO data

The ESPRESSO radial velocities observed between Julian Dates 2458524 and 2459341 have been made available by Faria et al. (2022). We analysed a set of 114 ESPRESSO velocities obtained from the stellar spectra by using a template matching algorithm. These velocities were accompanied by the respective full-width
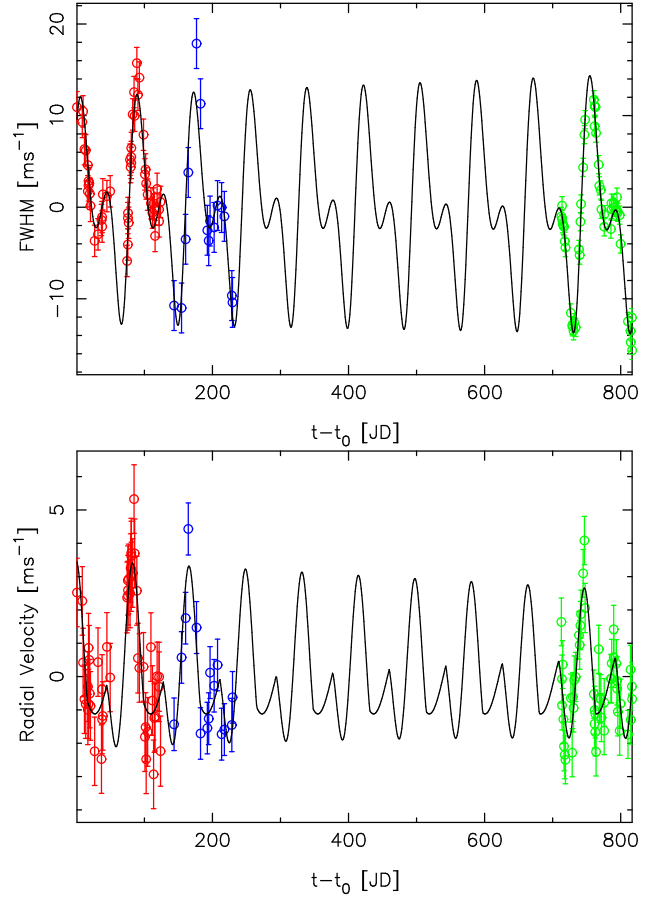
Fig. 1. Top panel: ESPRESSO FWHM values and their modelled variability (solid curve) according to the favoured model with two sinusoids. Bottom panel: Modelled RV variations caused by two spots on the stellar surface. Keplerian signals have not been subtracted from the bottom panel.

at half-maximum (FWHM) values. The precision of the instrument is highlighted by the average instrumental uncertainty of only 0.153 ms^{-1} but the radial velocities demonstrate variability of 2.015 ms^{-1} in standard deviation, which emphasises the fact that there are variations that can be resolved with the high-precision ESPRESSO data. As justified by Faria et al. (2022), we also divided the ESPRESSO data into three subsets (called E18, E19 and E21; Table 4) that were treated as independent data sets and analysed them in combination.

3.1. Analysis of ESPRESSO FWHM values

Our analysis of the FWHM values leads to the conclusion that there is evidence for periodic variability that can be modelled with two sinusoidal functions with periods near the reported rotation period of the star. These sinusoids have periodicities of 83.15±0.11 and 83.07±0.08 days, respectively, with a considerable phase difference as seen in Fig. 1. The periodicities align well with the known stellar rotation period, and can be interpreted as signatures of spots co-rotating on the stellar surface. They also correspond to independent estimates for the stellar rotation period. We attempted to model the FWHM data with harmonic periodicities but the double sinusoid model with periods around the stellar rotation period performed better.

3.2. Analysis of ESPRESSO radial velocities

The radial velocity signal of Proxima b is very confidently present in the ESPRESSO radial velocities. Our DRAM samplings revealed the global maximum corresponding to this signal very clearly and uniquely, as demonstrated in Fig. 2 (top panel). The local maxima correspond to a daily alias of the global maximum at a period of roughly 1.1 days and rotation-induced variability including its harmonics and aliases around periods of 80 and 40 days, respectively. Accounting for the signal of Proxima b and searching for additional periodicities leads to a clear identification of the groups of maxima around periods of 40 and 80 days, respectively (Fig. 2, middle panel). It appears clear that these maxima are caused by stellar rotation coupled with spot structures on the stellar surface (see Aigrain et al. 2012) and they are split into several modes due to aliasing caused by a large gap in the ESPRESSO data between JDs 2458753 and 2459236. Yet, some of the maxima could also be caused by differential rotation and spots at different latitudes (Wargelin et al. 2017).

The rotation-induced periodicities give rise to our attempts to model the corresponding variability with sinusoidal/Keplerian signals at either period or by applying the geometric spot model. The latter approach seems prominent because the functional form of the spot model has additive components with sinusoidal signals at periods $P_{\rm rot}$ and $P_{\rm rot}/2$ because there is the term $\sin x$ and also $\sin x \cos x = \frac{1}{2}\sin 2x$ for $x = \frac{2\pi t}{P} + \omega$. It thus appears natural that we observe maxima at these periods. According to (Aigrain et al. 2012), the latter periodicity, half of the rotation period of the star, can produce the highest apparent periodicity for simulated data as we indeed observe in Fig. 2.

We tabulate the probabilities of different models in Table 2 together with a summary of the signals they contain. Although the geometric spot was not the most probable of models with two periodic signals, it still performed reasonably well and was only beaten by a model containing a sinusoid with a period of 41 days. Our searches for a third periodicity revealed isolated maxima at periods of roughly 5 days and around 80 days. The latter periodicity again corresponds to the rotation period of the star, which makes it clear that more sophisticated models are needed to describe the rotation-induced variability (Fig. 2).

We thus tested models with Keplerian signals, sinusoids and spots and found an optimal combination for $k = 3$ to be a model containing the Keplerian signal of Proxima b at a period of 11.2 days and two spots (Table 2). This model left no discernible periodicities at or near the rotation period and its first harmonic (Fig. 3). The RV variability of these two spots is shown in Fig. 1 (bottom panel). An approximately equally probable model was found to be one that contained Keplerian or sinusoidal periodicities at 11.2, 41, and 83 days, corresponding to a model with Proxima b, rotation period of the star and its first harmonic. Therefore, it seems reasonable to state that effects of two spots explain the observed sets of maxima at and around 41 and 83 days as see in Fig. 2 (middle panel). We note that according to the geometric spot model, the observable effects of the spots are qualitatively different – one is visible over half of the time whereas the other is visible less than half of the time, which implies that the spots are on different stellar hemispheres. We note that as any periodic function can be presented as a sum of its Fourier components, it is natural that the model with first harmonic periodicities also produces the observed variability rather well.

We continued to search for additional signals while modelling the effects of the two spots and Proxima b. With a geometric model for the two spots and a Keplerian model for Proxima
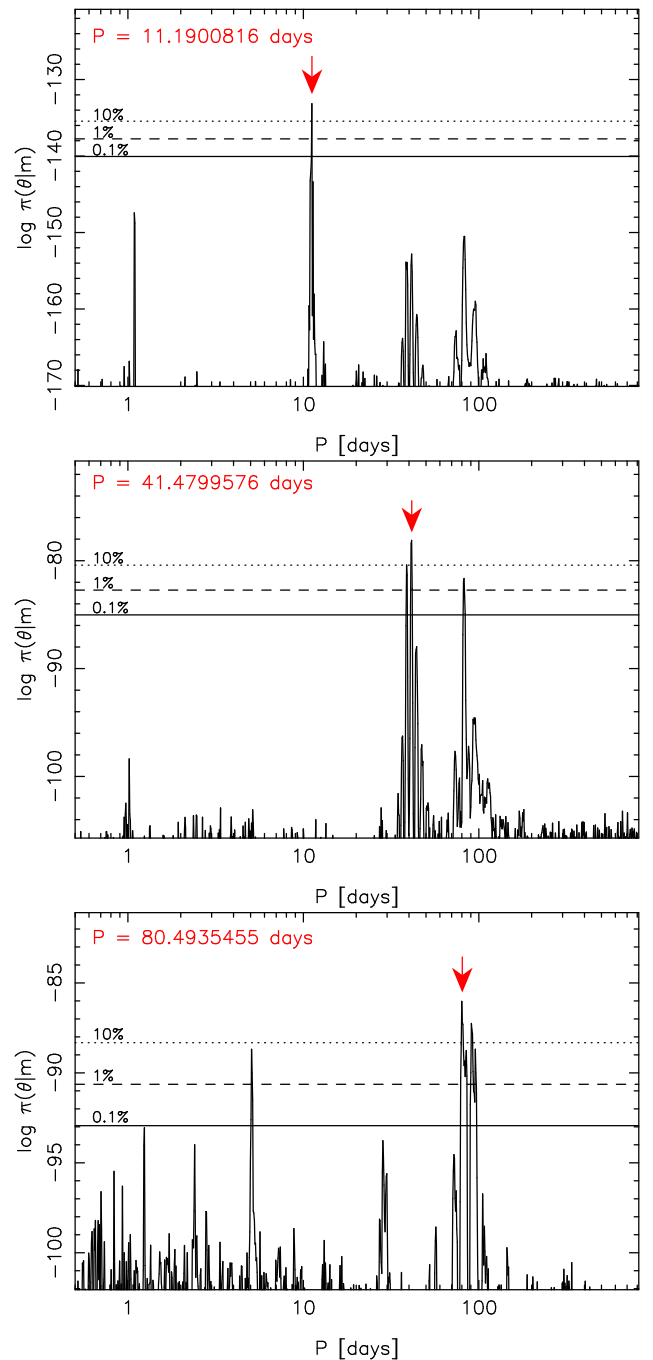

Fig. 2. Estimated posterior probability density as a function of the period parameter given models with $k = 1, 2, 3$ (top to bottom) Keplerian signals. The red arrows denote the global maxima and the horizontal lines denote the 10% (dotted), 1% (dashed), and 0.1% (solid) credibility intervals with respect to the maxima.

b, our searches with $k = 4$ identified the signal of the candidate planet Proxima d reported by Faria et al. (2022) at the period of 5.1237 ± 0.0022 days as a unique and significant probability maximum (Fig. 3, top panel) consistently with the results of Faria et al. (2022). For $k = 5$, the most prominent probability maximum was identified at a period of 0.628 days but the Bayes factor approximated based on BIS values corresponding to this solution was not in excess of our detection threshold of $\beta = 150$.

The model with harmonic periodicities at roughly $P_{\rm rot}$ and $P_{\rm rot}/2$ enabled identifying the candidate d as well (Fig. 4, top panel) but did not fully account for the rotation-induced vari-

Table 2. Model probability matrix for models with different Keplerian signals, sinusoidal signals, and physical spot-induced signals. The probabilities have been scaled such that their sum is unity for this model set. Parameter k denotes the overall number of signals in each model. The periods of each signal are also shown in the order of significance. The column titled Full denotes a model where all parameters are treated as free parameters of the model. Simplified denotes models for which all unnecessary components have been removed from the model decreasing the model complexity and thus increasing the probability. The models have free parameters ranging from 9 for $k = 0$ to 43 for $k = 6$. The period of spot-induced signals always corresponds to the stellar rotation period albeit allowing for small differences due to differential rotation.

k	Keplerian P (days)	Sinusoid P (days)	Spots	Full Probability	Simplified Probability
0	–	–	–	1.4×10^{-40}	3.4×10^{-37}
1	11.2	–	–	5.1×10^{-30}	3.9×10^{-25}
2	11.2	83	–	5.4×10^{-29}	1.5×10^{-26}
2	11.2	41	–	2.0×10^{-19}	8.4×10^{-14}
2	11.2	–	1	3.0×10^{-22}	8.9×10^{-18}
2	11.2, 41	–	–	2.2×10^{-21}	8.4×10^{-14}
2	11.2, 83	–	–	4.5×10^{-23}	2.1×10^{-18}
3	11.2	83	1	3.4×10^{-18}	1.3×10^{-13}
3	11.2	–	2	7.3×10^{-16}	1.0×10^{-11}
3	11.2	41, 83	–	2.9×10^{-16}	2.2×10^{-12}
3	11.2, 41, 83	–	–	1.2×10^{-19}	6.3×10^{-12}
3	11.2, 5.1	–	1	6.4×10^{-23}	4.6×10^{-16}
4	11.2, 5.1	83	1	3.2×10^{-17}	1.3×10^{-10}
4	11.2, 5.1	–	2	1.2×10^{-14}	4.3×10^{-8}
4	11.2, 41, 83, 5.1	–	–	1.3×10^{-16}	8.3×10^{-9}
5	11.2, 5.1, 29	83	1	7.0×10^{-16}	3.0×10^{-7}
5	11.2, 5.1, 0.6	–	2	4.4×10^{-15}	4.5×10^{-6}
5	11.2, 41, 83, 5.1, 29	–	–	5.1×10^{-15}	7.5×10^{-5}
6	11.2, 5.1, 29, 0.6	83	1	7.2×10^{-13}	5.8×10^{-4}
6	11.2, 5.1, 29, 1.7	83	1	3.7×10^{-14}	1.4×10^{-4}
6	11.2, 5.1, 29, 2.4	83	1	1.4×10^{-13}	2.3×10^{-4}
6	11.2, 41, 83, 5.1, 29, 0.6	–	–	1.5×10^{-11}	0.667
6	11.2, 41, 83, 5.1, 29, 1.7	–	–	2.1×10^{-12}	0.272
6	11.2, 41, 83, 5.1, 29, 2.4	–	–	6.0×10^{-14}	0.060

ability and left some probability maxima near $P_{\rm rot}/3$ seen in Fig. 4 (bottom panel). We thus included the third rotational harmonic in the model and found that the resulting $k = 5$ model had a significantly elevated probability (Table 2). The signal at a period of 28.6 days is reasonably close to one third of the rotation period of the star, which is what can be expected to be produced by spots (Aigrain et al. 2012). Although this periodicity does not exactly coincide with one third of the star's observed rotation period of 83 days, it is certainly consistent with it given that the apparent photometric variations of the star change seasonally and range from 77.1 to 90.1 days as an indication of differential rotation (Wargelin et al. 2017).

The joint effects of several spots on the RV variability could lead to a situation where simple physically motivated spot models coupled with differential rotation are not necessarily the most accurate ones. This is probably the case for Proxima Centauri, too, as seen in the TESS full-frame light curve presented in Vida et al. (2019) that demonstrates spot-induced long-term variability which is too complex to be explained by a simple spot model. Indeed, for $k = 5$ we find that sinusoidal variations at roughly $P_{\rm rot}$, $P_{\rm rot}/2$ and $P_{\rm rot}/3$ together with Keplerian signals of Proxima b and d yield the most probable description of the data (2). This model can be considered to represent an empirical model of the rotation-induced variability and planets in the system.

The results from periodicity searches with $k = 6$ provide evidence of additional signals. Our DRAM samplings identified

maxima at periods of 0.628, 1.700 and 2.420 days (Fig. 5) but it is not immediately clear which one of them represents a true signal and which ones are aliases. For an aliasing frequency of f_a and an underlying signal at a frequency of f_s, signals can appear at frequencies of $f_s \pm n f_a$, for $n = 0, 1, \ldots$. This seems to be the case here as well because, for instance, a signal at 1.700 days would lead to first-order aliases at 2.428 and 0.628 days, respectively – fully explaining the observed pattern of maxima in Fig. 5 (bottom panel). Similarly, true signals at periods of 0.628 or 2.420 days would produce the observed pattern with at most second-order aliases. It therefore seems apparent that all the observed maxima are caused by a single underlying periodicity. Based on the available ESPRESSO data, it is not possible to distinguish the real periodicity from its aliases. However, the underlying signal must be a true periodicity – random noise would not produce a pattern of probability maxima that match the periods caused by simple aliasing.

We note that although the overall pattern is rather clear, the exact relative heights of the probability maxima in Fig. 5 depend on how efficiently each of the maxima was sampled with our MCMC samplings. Typically, shorter periodicities have narrower maxima, making identifying their positions accurately computationally more time-consuming. Yet, we find the maximum corresponding to the shortest periodicity of 0.628 days to represent the most probable solution given the data. This can be seen in Table 2 where we have compared each of the probability
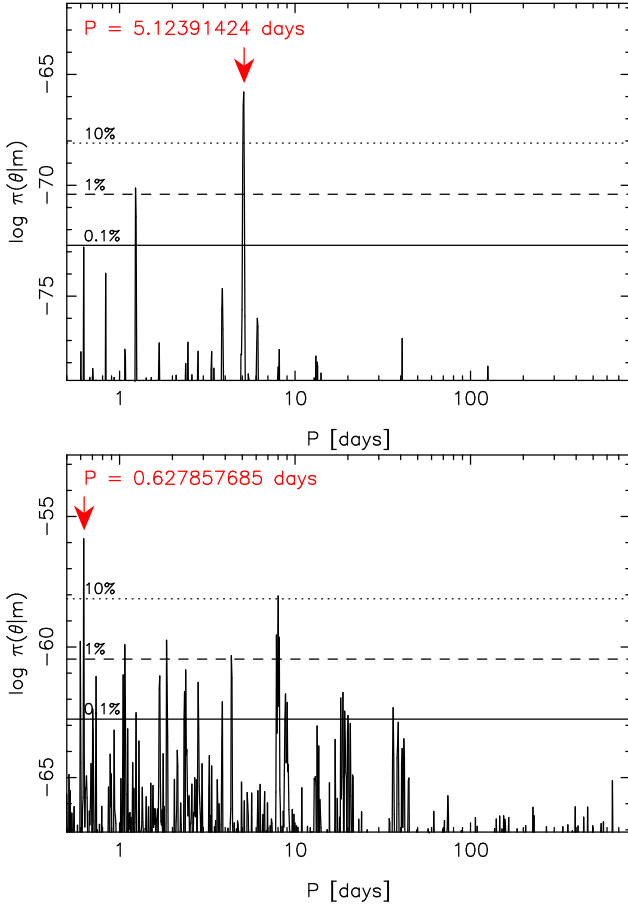
Fig. 3. As in Fig. 2 but for $k = 4$ (top) and $k = 5$ (bottom) given the model with two spots.

Fig. 4. As in Fig. 2 but for $k = 4$ and $k = 5$ when modelling the rotation-induced variability as a series of approximate harmonics. The 28.6-day signal corresponds to the $P_{rot}/3$ harmonic.

maxima by assuming they constitute separate models. The interpretation that the signal at the period of 0.628 days is a true periodicity is also supported by the fact that it corresponds to the highest maximum given the spot model (Fig. 3).

3.3. RV signatures of spots

Although models with $k = 5$ and $k = 6$ were favoured in our analyses, we rely on the simpler model with $k = 4$ to assess properties spot signatures. We adopt the estimated inclination from Klein et al. (2021) as prior information such that we assume it to have a Gaussian distribution with mean and standard deviation corresponding to the estimated 47 deg and the uncertainty of 7 deg, respectively. We can then obtain probability densities for the parameters of the spots in our model (Eq. 6).

The signatures of the two spots are shown in Fig. 6 as phase-folded signals because we assumed the spots to not appear to undergo significant evolution over the baseline of the ESPRESSO data. We have tabulated the relevant parameters of these spots in Table 3. Qualitatively, it is easy to notice that the two spots are on different hemispheres of the star. This is because one is visible only about one third of the time whereas the other is visible over half of the time. The time-differences in visibility enable determining the respective latitudes of the spots, albeit with high uncertainties (Table 3). Moreover, the estimated periods of the two spots are different, which is positive evidence for the existence of differential rotation.
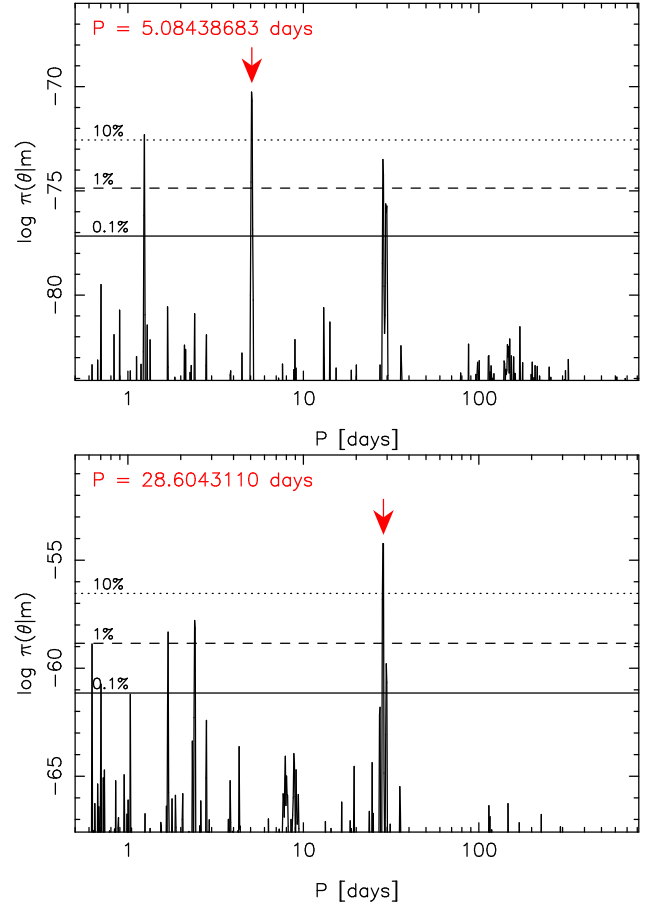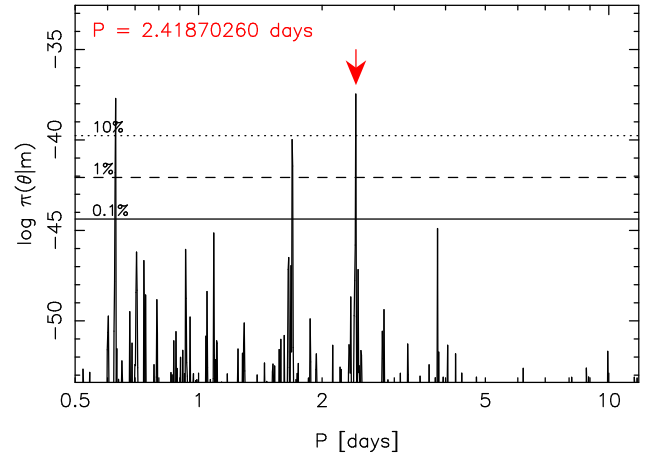

Fig. 5. As in Fig. 2 but for a model with $k = 6$ where the rotation-induced variability has been modelled with periodicities at roughly P_{rot}, $P_{rot}/2$ and $P_{rot}/3$. The three maxima are caused by daily aliasing of one underlying signal.

4. Combined data

The combined data set consists of radial velocities from three instruments. However, as was the choice for ESPRESSO, we treated subsets of HARPS data, too, as independent data sets because there was data taken with different cadences during different observing programmes. For instance, the oldest HARPS data taken between May 2004 and March 2013 by Mayor et al.

Table 3. Estimated spot parameters for Proxima Centauri given *a priori* known probability distribution for the stellar inclination. The values are maximum *a posteriori* estimates, standard errors, and 99% credibility intervals.

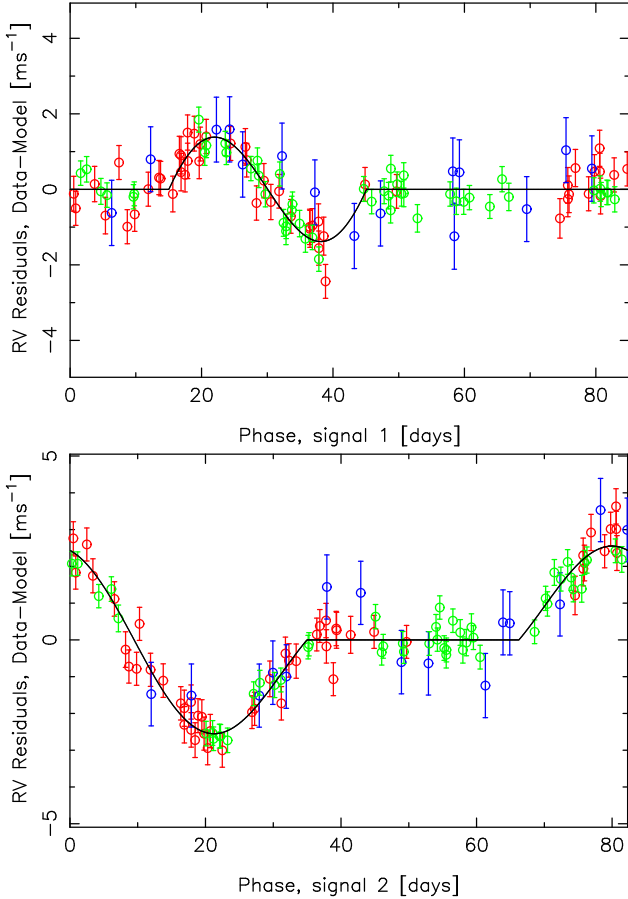| Parameter	Spot 1	Spot 2
P (days)	85.15±0.20 [84.59, 85.72]	82.40±0.22 [81.78, 83.04]
A (ms^{-1})	-15.7±4.3 [-22.9, -0.6]	-7.5±1.2 [-11.0, -4.4]
ψ (rad)	-0.38±0.17 [-0.88, 0.12]	0.45±0.15 [0.09, 0.86]
ϕ (rad)	2.22±0.12 [1.86, 2.54]	0.63±0.13 [0.24, 0.95]
i (rad)	0.82±0.13	[0.54, 1.22]

Fig. 6. The RV signals of two spots in the ESPRESSO data. The solid curves represent the model solution and the red, blue, and green filled circles denote the three ESPRESSO subsets (Faria et al. 2022).

and Bonfils et al. (ESO programme IDs 072.C-0488(E), 183.C-0437(A), and 082.C-0718(B)) was taken with a reasonably low cadence, enabling probing frequencies on time scales from days to years. On the other hand, the two high-cadence Cool Tiny Beats campaigns (CTB1 and CTB2) of Anglada-Escudé et al. (191.C-0505(A)) in May and December 2013, respectively, were aimed at detecting variations within and between nights. Finally, the Pale Red Dot (PRD) campaign of Anglada-Escudé et al. (096.C-0082(A-F)) designated to confirm Proxima b (Anglada-Escudé et al. 2016) from January to April 2016, and the Red Dots (RD) campaign of Anglada-Escudé et al. (099.C-0880(A)) from May to September 2017, were mainly aimed at daily to monthly cadences. We thus model each of these data sets as independent ones. This leads to a combined set of nine independent data sets.

We processed the HARPS data products with the algorithms of Anglada-Escudé & Butler (2012) to obtain velocities and ac-tivity indicators. The UVES data was included in the analysis as published in Butler et al. (2019). The properties of data subsets from the three instruments are tabulated in Table 4.

For the standard HARPS velocities as derived for M dwarfs (Anglada-Escudé & Butler 2012), we consider three activity in-dicators, namely, bisector span (BIS), FWHM, and CaII H&K emission. However, we also adopt another set of activity prox-ies called differential velocities (Feng et al. 2017). These proxies are derived as a difference between velocities calculated for sub-sets of HARPS apertures, i.e., velocities calculated for different wavelength ranges. This implies that any wavelength invariant Keplerian signals are subtracted from the proxies but all wave-length dependent variability remains. We obtain the differential velocities such that we neglect the 24 bluest HARPS apertures due to their higher noise levels for typical M dwarfs (Anglada-Escudé & Butler 2012), and calculate the velocities for the 24 reddest apertures as well as the 24 middle apertures. The differ-ences between these velocities are then used as the noise proxies for both radial velocities derived for the red and middle apertures that we treat as independent data sets.

Adopting the three near-harmonic periodicities to account for the rotation-induced variations in the ESPRESSO data, and the best description of HARPS and UVES velocities identified similarly as for ESPRESSO, we obtained samples from the pos-terior densities of models with $k = 0, ..., 3$ Keplerian signals given the full data set. These signals corresponded to the three re-ported candidate planets and the trio of aliasing periodicities that we identified in ESPRESSO data. According to our results, the signals corresponding to Proxima b and d at periods of roughly 11.2 and 5.1 days, respectively, are well supported by data (Table 5). The signal of the proposed long-candidate Proxima c was not found to be credibly present at a period of approximately 1900 days. This is evident based on the model probabilities in Table 5. Yet, the combined data, too, provides support for another short-period signal that can be interpreted as evidence for a candidate planet. This signal at the period of 0.6285453±0.0000078 days with an amplitude of 0.205±0.042 ms^{-1} corresponds to a can-didate planet with a minimum mass of only 0.067±0.014 M$_\oplus$. We have tabulated the estimated Keplerian parameters in Table 6 and plotted the phase-folded signals in Fig. 7. The estimated periods of the two alternative solutions for the 6th signal are 1.700212±0.000071 and 2.42039±0.00027 days corresponding to minimum masses of 0.111±0.018 and 0.090±0.025 M$_\oplus$, re-spectively.

To see whether the signals at periods of 5.1 and 0.6 days were supported by HARPS data, we adopted the global solutions corresponding to models with $k = 1, ..., 3$ and tested whether the likelihood of HARPS data increased significantly. For the 5.1-day signal, the joint HARPS likelihood increased by 10.65 on the logarithmic scale, which is caused by pure chance with a probability of only 0.012. This implies that candidate Proxima

Table 4. Properties of the radial velocity data sets from ESPRESSO, HARPS, and UVES. Numbers of data (N), first and last epochs (T_1 and T_N), and data baselines (ΔT).

| Instrument	Data set	N	T_1 (JD-2450000)	T_N (JD-2450000)	ΔT (days)
UVES	All	210	1634.72	3823.62	2188.90
HARPS	Old	66	3152.60	6374.76	3222.16
HARPS	CTB1	164	6417.50	6428.53	11.03
HARPS	CTB2	23	6656.80	6667.86	11.06
HARPS	PRD	56	7406.87	7479.89	73.02
HARPS	RD	66	7905.47	8027.48	122.01
ESPRESSO	E18	50	8524.86	8647.71	122.85
ESPRESSO	E19	15	8667.58	8753.47	85.89
ESPRESSO	E21	49	9236.86	9340.86	104.00
All		699	1634.72	9340.86	7706.14
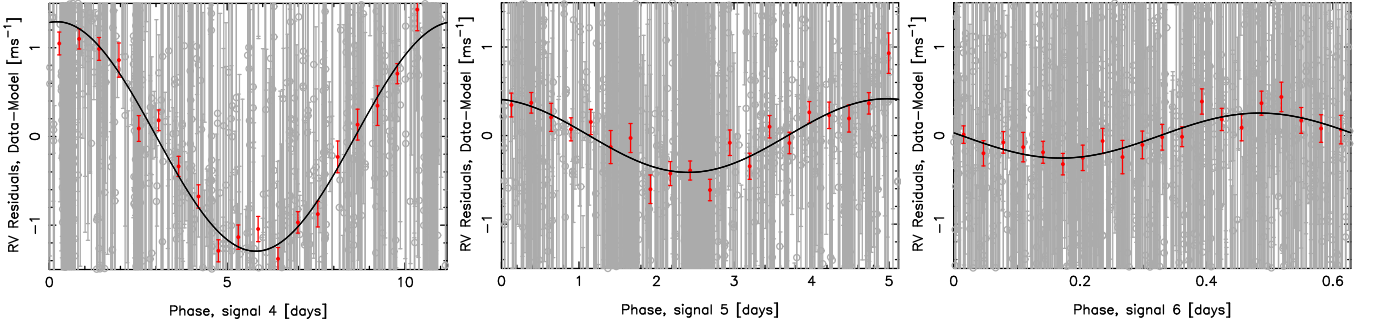
Fig. 7. Phase-folded radial velocity signals of the candidate planets. The radial velocity data are shown as gray circles in the background and the red filled circles denote weighted means. The signals 4, 5, and 6 denote candidates b, d, and e. Numbers 1-3 have been reserved for the rotational harmonics in the current model.

Table 5. Probabilities of models with different numbers of signals given the full data set. The periods of the signals in each model are shown in the second column. The models have been simplified as in the last column of Table 2. The spot-induced variations are modelled as three near-harmonic periodicities for the ESPRESSO data.

k	P (days)	Probability
0	–	6.2×10^{-47}
1	11.2	1.6×10^{-10}
2	11.2, 5.1	1.1×10^{-3}
3	11.2, 5.1, 0.6	0.658
3	11.2, 5.1, 1.7	0.333
3	11.2, 5.1, 2.4	8.2×10^{-3}
3	11.2, 5.1, 1900	1.3×10^{-5}

d gains some independent support from HARPS observations. The same test for the 0.6-day signal gives a probability of 0.117, which does not enable concluding that HARPS data provides supporting evidence for the signal.

5. Search for transits in the TESS photometry

We searched for signatures of transits of the postulated short-period candidate in TESS data as obtained from the Mikulski Archive for Space Telescopes. However, the data was contaminated with flares, and we therefore modelled the flare morphology in order to remove their effects from the light curves.

Our empirical flare model consists of two parts: a half Gaussian rise and an exponential decay phase, as described in Pitkin et al. (2014). The decay phase was modelled as a double exponential because Davenport et al. (2014) noted that different physical processes dominate separate regimes in decay phase. The flare model was fitted to the data by obtaining samples with Metropolis-Hastings algorithm near every candidate flare event. For instance, for TESS sector 11, we identified and modelled 45 flare candidates, from which 6 were rejected after model comparisons. 29 single flare events (classical flares) were accepted. As suggested by Davenport et al. (2014), more complex flare events were modelled with superposition of several classical subflares. Ten such events were accepted in model comparisons. Finally, the accepted flares were subtracted from the original light curve. These flares and their identification process will be discussed further in Koistinen et al. (2023).

After removing the flares, we subjected the residual data to transit searches by applying the EMPEROR code (Peña Rojas et al. 2023; Vinés et al. 2023). We could not identify any features resembling transits at or near the identified periods in the available data from three TESS sectors.

6. Discussion

We have demonstrated that Proxima Centauri is probably surrounded by a system of small planets with low minimum masses. Our results align with the conclusions of Faria et al. (2022) that there is another small planet in the system interior to the orbit of Proxima b. Our results are consistent with a lack of evidence for the postulated outer planet Proxima c (Artigau et al. 2022).

Table 6. Maximum *a posteriori* estimates and standard errors of the available Keplerian parameters given the combined radial velocity data. The uncertainties of the semi-major axis *a* and minimum mass $m_p \sin i$ have been estimated by accounting for the uncertainty in the stellar mass.

Parameter	Candidate b	Candidate d	Candidate e
P (days)	11.18482±0.00062	5.12391±0.00033	0.6285453±0.0000078
K (ms^{-1})	1.306±0.060	0.381±0.043	0.205±0.042
ω (rad)	1.3±1.1	1.2±0.8	2.7±0.5
e	0.004±0.019	0.007±0.047	0.061±0.045
M_0 (rad)	1.6±1.1	1.4±0.7	1.7±0.6
$m_p \sin i$ (M$_\oplus$)	1.117±0.053	0.251±0.029	0.067±0.014
a (au)	0.04842±0.00030	0.02877±0.00018	0.00710±0.00005

Yet, we have also demonstrated that the ESPRESSO data are modelled well by adopting a model with a total of six periodic signals. While Proxima b and d serve as credible explanations for two of them, a nearly harmonic set of periodicities at 83, 41, and 29 days probably arises from the stellar differential rotation coupled with spots at different latitudes. These spots can also be modelled with a geometric spot model that roughly enables latitude determination.

The sixth signal, albeit a weak one, seems more likely to be caused by another planet orbiting the star but its exact period remains to be distinguished from the aliases and its significance verified with future data. However, the very detection of this prominent signal suggests that detections of radial velocity signals with amplitudes of 0.2 ms^{-1} are possible. Coincidentally, this is approximately only a factor of 2 greater than the amplitude of a radial velocity signal of an Earth analog around a Sun-like star.

No corresponding periodicities in the available ESPRESSO activity indicators have been reported near the observed short periodicities (Faria et al. 2022) and they are not related to the stellar rotation period. This leads us to suggest that they represent the detection of a candidate planet with a minimum mass comparable to that of Mars.

We also obtain evidence for two significant spots on the surface of Proxima Centauri. When modelling the data with a geometric spot model. These spots appear to occur at both sides of the stellar equator (Fig. 6). The spot properties are only weakly constrained by adopting an inclination prior and assuming the inclination of 47±7 deg (Klein et al. 2021) is correct. This is because the latitudes of the spots are primarily constrained by the fact that one is visible over half of the rotation period while the other is visible less than half of the period. Similar constraints arise when one of the spots is modelled as a sinusoid and implicitly assuming it is constantly visible.

It is conceivable that the effect of spots on the radial velocities remains constant throughout the ESPRESSO data baseline of 816 days. Although it is well-known that starspots evolve over a period of few rotation periods (e.g. Ioannidis & Schmitt 2020), photometric observations of Proxima Centauri have demonstrated that active longitudes on the stellar surface remain remarkably stable for years (Wargelin et al. 2017). Although not explicitly mentioned in the model comparison matrix (Table 2), we also tested whether ESPRESSO data showed any evidence for spot evolution. The model parameters were found to be consistent on both sides of the large gap in the data and no significant change could be observed given rather large uncertainties.

Young, rapidly rotating fully convective stars seem to retain their spot structures on time-scales much longer than their rotation periods (Davenport et al. 2015; Robertson et al. 2020), but this is not necessarily the case for slowly rotation stars such as Proxima Centauri. Yet, we observe no evidence for statistically significant differences in the modelled spot pattern over the baseline of the ESPRESSO data, which indicates that the largest spot structures probably remain approximately constant over several rotation periods for Proxima Centauri

We searched for transits of the proposed Proxima e in TESS data at each of the candidate periods reported in the current work, as well as at the period of Proxima d. No prominent transit events were identified.

Acknowledgements

References

Abrevaya, X. C., Leitzinger, M., Oppezzo, O. J., Odert, P., et al. 2020, MNRAS, 494, L69
Aigrain, S., Pont, F., & Zucker, S. 2012, MNRAS, 419, 3147
Andersen, J. M. & Korhonen, H. 2015, MNRAS, 448, 3053
Anglada, G., Amado, P. J., Ortiz, J. L., Gómez, J. F., et al. 2017, ApJ, 850, L6
Anglada-Escudé, G. & Butler, R. P. 2012, ApJS, 200, 15
Anglada-Escudé, G. & Tuomi, M. 2015, Science, 347, 1080
Anglada-Escudé, G., Amado, P. J., Barnes, J., Berdiñas, Z. M., et al. 2016, Nature, 536, 437
Artigau, E., Cadieux, C., Cook, N. J., Doyon, R., et al. 2022, AJ, accepted (arXiv:2207.13524)
Benedict, G. F., McArthur, B., Nelan, E., Story, D., et al. 1998, AJ, 116, 429
Benedict, G. F. & McArthur, B. E. 2020, RNAAS, 4, 86
Bixel, A. & Apai, D. 2017, ApJ, 836, L31
Blank, D. L., Feliz, D., Collins, K. A., White, G. L., et al. 2018, AJ, 155, 228
Boutle, I. A., Mayne, N. J., Drummond, B., Manners, J., et al. 2017, A&A, 601, A120
Boyajian, T. S., von Braun, K., van Belle, G., McAlister, H. A., et al. 2012, ApJ, 757, 112
Butler, R. P., Vogt, S. S., Laughlin, G., et al. 2017, AJ, 153, 208
Butler, R. P., Jones, H. R. A., Feng, F., Tuomi, M., et al. 2019, AJ, 158, 251
Collins, J. M., Jones, H. R. A., & Barnes, J. R. 2017, A&A, 602, A48
Cumming, A. 2004, MNRAS, 354, 1165
Damasso, M. & Del Sordo, F. 2017, A&A, 599, A126
Damasso, M., Del Sordo, F., Anglada-Escudé, G., Giacobbe, P., et al. 2020, SciA, 6, eaax7467

Davenport, J. R. A., Hawley, S. L., Hebb, L., Wisniewski, J. P., et al. 2014, ApJ, 797, 122

Davenport, J. R. A., Hebb, L., & Hawley, S. L. 2015, ApJ, 806, 212

Davenport, J. R. A., Kipping, D. M., Sasselov, D., Matthews, J. M., & Cameron, C. ApJ, 829, L31

Del Genio, A. D., Way, M. J., Amundsen, D. S., Aleinov, I., et al. 2019, Astrobiology, 19, 99

Díaz, M. R., Jenkins, J. S., Tuomi, M., et al. 2018, AJ, 155, 126

Dumusque, X. 2014, ApJ, 796, 133

Dumusque, X., Borsa, F., Damasso, M., et al. 2017, A&A, 598, 133

Faria, J. P., Suárez Mascareño, A., Figueira, P., Silva, A. M., et al. 2022, A&A, 658, A115

Feng, F., Tuomi, M., Jones, H. R. A., Butler, R. P., & Vogt, S. S. 2016, MNRAS, 461, 2440

Feng, F., Tuomi, M., Jones, H. R. A., Barnes, J. R., et al. 2017, AJ, 154, 135

Ford, E. B. 2006, ApJ, 642, 505

Gaia Collaboration 2021, A&A, 649, A1

Garraffo, C., Alvarado-Gomez, J. D., Cohen, O., & Drake, J. J. 2022, ApJ, 941, L8

Gelman, A., Carlin, J. B., Stern, H. S., & Rubin D. B. 2003, Bayesian Data Analysis (New York: Chapman & Hall)

Gilbert, E. A., Barclay, T., Kruse, E., Quintana, E. V., & Walkowich, L. M. 2021, Front. Astron. Space Sci., 19, 769371

Gratton, R., Zurlo, A., Le Coroller, H., Damasso, M., et al. 2020, A&A, 638, A120

Haario, H., Saksman, E., & Tamminen, J. 2001, Bernoulli, 7, 223

Haario, H., Laine, M., Mira, A., and Saksman, E. 2006, Statistics and Computing, 16, 339

Hastings, W. 1970, Biometrika 57, 97

Herath, M., Gunesekera, S., & Jayaratne, C. 2021, MNRAS, 500, 333

Howard, W. S., Tilley, M. A., Corbett, H., Youngblood, A., et al. 2018, ApJ, 860, L30

Ioannidis, P. & Schmitt, H. M. M. 2020, A&A, 644, A26

Jenkins, J. S., Harrington, J., Challener, R. C., Kurtovic, N. T., et al. 2019, MNRAS, 482, 268

Kane, S. R., Gelino, D. M., & Turnbull, M. C. 2017, AJ, 153, 52

Käpylä, P. J. 2021, A&A, 651, A66

Kass, R. E. & Raftery, A. E. 1995, J. Am. Stat. Ass., 430, 773

Kervella, P., Thévenin, F., & Lovis, C. 2017, A&A, 598, L7

Kervella, P., Arenou, F., & Schneider, J. 2020, A&A, 635, L14

Kervella, P., Arenou, F., & Thévenin, F. 2022, A&A, 657, A7

Kipping, D. M., Cameron, C., Hartman, J. D., Davenport, J. R. A., et al. 2017, AJ, 153, 93

Kiraga, M. & Stepien, K. 2007, Acta Astronomica, 57, 149

Klein, B., Donati, J.-J., Hébrard, E. M., Zaire, B., et al. 2021, MNRAS, 500, 1844

Koistinen, K., Tuomi, M., Hackman, T., et al. 2023, in preparation.

Korhonen, H., Andersen, J. M., Piskunov, M., Hackman, T., et al. 2014, MNRAS, 448, 3038

Lee, Y., Dong, C., & Tenishev, V. 2021, ApJ, 923, 190

Liddle, A. R. 2007, MNRAS, 377, L74

Lisogorskyi, M., Boro Saikia, S., Jeffers, S. V., Jones, H. R. A., et al. 2020, MNRAS, 497, 4009

Liu, H.-G., Jiang, P., Huang, X., Yu, Z.-Y., et al. 2018, AJ, 155, 12

Lomb, N. R. 1976, Astrophys. Space Sci., 39, 447

MacGregor, M. A., Weinberger, A. J., Wilner, D. J., Kowalski, A. F., & Cranmer, S. R. 2018, ApJ, 855, L2

Mann, A. W., Feiden, G. A., Gaidos, E., Boyajian, T., & von Braun, K. 2015, ApJ, 804, 64

Mann, A. W., Feiden, G. A., Gaidos, E., Boyajian, T., & von Braun, K. 2016, ApJ, 819, 87

Meadows, V. S., Arney, G. N., Schwieterman, E. W., Lustig-Yaeger, J., et al. 2019, Astrobiology, 18, 133

Mesa, D., Zurlo, A., Milli, J., Gratton, R., et al. 2017, MNRAS, 466, L118

Metropolis, N., Rosenbluth, A. W., Rosenbluth, M. N., et al. 1953, J. Chem. Phys., 21, 1087

Noack, L., Kislyakova, K. G., Johnstone, C. P., Güdel, M., & Fossati, L. 2021, A&A, 651, A103

Pavlenko, Y., Suárez Mascareño, A., Rebolo, R., Lodieu, N., et al. 2017, A&A, 606, A49

Pavlenko, Y., Suárez Mascareño, A., Zapatero, O. M. R., Rebolo, R., et al. 2019, A&A, 626, A111

Peña Rojas, P., Jenkins, J., Vinés, J., et al. 2023, in preparation.

Pitkin, M., Williams, D., Fletcher, L., & Grant S. D. T. 2014, MNRAS, 445, 2268

Reiner, A., Bean, J. L., Huber, K. F., Dreizler, S., et al. 2010, ApJ, 710, 432

Ribas, I., Bolmont, E., Selsis, F., Reiners, A., et al. 2016, A&A, 596, A111

Ribas, I., Gregg, M. D., Boyajian, T. S., & Bolmont, E. 2017, A&A, 603, A58

Robertson, P., Stefansson, G., Mahadevan, S., Endl, M., et al. 2020, ApJ, 897, 125

Scargle, J. D. 1982, ApJ, 263, 835

Suárez Mascareño, A., Rebolo, R., & González Hernández J. I. 2016, A&A, 595, A12

Suárez Mascareño, A., Faria, J. P., Figueira, P., Lovis, C., et al. 2020, A&A, 639, A77

Tuomi, M., Jones, H. R. A., Barnes, J. R., Anglada-Escudé, G., et al. 2018, AJ, 155, 192

Vida, K., Oláh, K., Kővári, Z., Driel-Gesztelyi, L., et al. 2019, ApJ, 884, 160

Vinés, J., Jenkins, J. S., et al. 2022, in preparation

Wargelin, B. J., Saar, S. H., Pojmański, G., Drake, J. J., & Kashyap, V. L. 2017, MNRAS, 464, 3281

Yadav, R. K., Christensen, U. R., Wolk, S. J., & Poppenhaeger, K. 2016, ApJ, 833, L28

Zic, A., Murphy, T., Lynch, C., Heald, G., et al. 2020, ApJ, 905, 23